Constrained growth of ultrasmall BiOCl nanodiscs with a low percentage of exposed {001} facets and their enhanced photoreactivity under visible light irradiation

CrossMark

Xiaofeng Chang [a,1], Shuangbao Wang [a,1], Qi Qi [b,1], M.A. Gondal [c], S.G. Rashid [c], Deyuan Yang [d], M.A. Dastageer [c], Kai Shen [d], Qingyu Xu [e], Peng Wang [a,*]

[a] National Laboratory of Solid State Microstructures, College of Engineering and Applied Sciences and Collaborative Innovation Center of Advanced Microstructures, Nanjing University, Nanjing 210093, China
[b] School of Chemistry and Chemical Engineering, Southeast University, Nanjing 211189, China
[c] Physics Department and Center of Excellence in Nanotechnology, King Fahd University of Petroleum and Minerals, Dhahran 31261, Saudi Arabia
[d] College of Materials Science and Technology, Nanjing University of Aeronautics and Astronautics, Nanjing 211100, China
[e] Department of Physics, Southeast University, Nanjing 211189, China

ARTICLE INFO

ABSTRACT

Tailored crystal growth of two dimensional (2D) structured BiOCl photocatalyst is a quite challenging area and prerequisite for achieving superior photoreactivity. In this work, the constrained growth of ultrasmall BiOCl nanodiscs (∼65 nm in diameter) with a low percentage of exposed {0 0 1} facets (as low as ∼59%) has been achieved through a facile hydrolysis route at normal temperature and pressure, by using sodium bismuthate ($NaBiO_3$) and hydroxylammonium chloride ($HONH_2 \cdot HCl$) aqueous solution as the bismuth source and "four-in-one" reaction media, respectively. By means of diverse characterization techniques and density functional theory (DFT) method, it was found that hydroxylammonium chloride solution not only acts as a kind of solvent, reductant and chloride donor, but also plays a crucial role on the constrained growth of {0 0 1} facets in BiOCl nanodiscs via the two-stage growth mechanism. Additionally and more importantly, the as-prepared BiOCl nanodiscs exhibit superior sorption capacity and visible-light-induced photodegradation performance of Rhodamine B contaminant, to the conventional BiOCl nanosheets dominated with {0 0 1} facets.

1. Introduction

Solar energy is quite simply the energy that is trapped from the sun's rays. A great deal of effort has been put into semiconductor photocatalysts which hold promise for many applications in environmental remediation and solar energy utilization [1–3].

Bismuth oxychloride (BiOCl) has already been demonstrated as an important material for environmental remediation and power source [4–10], owning to its efficient photoreactivity and unique structure. It is crystallized into layered structure where the [—O—Bi—O—Bi—O—] slabs are stacked above the other by Van der Waals forces through the Cl atoms along the *c*-axis [4]. The hydrolysis route based on the Bi^{3+}-Cl^- aqueous system is extensively regarded as the fundamental step during the crystal growth of BiOCl

sheet-like crystals in aqueous phase [11–13]. However, traditional hydrolysis method gives larger size distribution of BiOCl crystals and the diameter of these BiOCl sheet-like crystals usually lies in microsize.

As an important environmental and energy material, uniform and highly pure BiOCl single crystals with tailored crystallographic facets are vital and desirable. During the past few years, an exponential growth of efforts has been made to prepare BiOCl crystals with controllable size and morphology. Since the first report on the solvothermal preparation of BiOCl crystals in early 2002 [14], various strategies have been substantially developed [15–20]. Recently, a few attempts on the crystal facet engineering of BiOCl nanocrystals have been made as well. Xiong et al. [4] reported a mannitol-assisted hydrothermal route for the preparation of square edged two dimensional (2D) BiOCl nanoplates. Mannitol molecules direct the layered structure of BiOCl into a plate-growth for the rapid growth along the [001] direction. The hydrogen bonding between hydroxyl groups and its selective adsorption

also benefits to the formation to regular square-like nanoplates. Song et al. [21] prepared hierarchical structured BiOCl crystals with controllable thickness via a pyridine-mediated solvothermal route. It was found that the thickness of the BiOCl nanoplates decreases with reducing the volume ratio. A basic lone pair of electrons from the nitrogen atom competes with Cl^- in the formation process of BiOCl, influencing the ultimate shape of the BiOCl crystals. Ma et al. [22] reported the preparation of ultrathin BiOCl nanoflakes through an ionothermal technique under the structural direction of 1-hexadecyl-3-methylimidazolium chloride ($[C_{16}Mim]Cl$)·$[C_{16}Mim]^+$ cations, which is preferably adsorbed on the ab plane of BiOCl, may inhibit the growth along the [0 0 1] direction of BiOCl. Wang et al. [23] prepared BiOCl microflowers assembled by thin BiOCl nanosheets through a glycerol-mediated solvothermal path. The growth in the [0 0 1] direction is suppressed due to the binding of glycerol molecules onto (0 0 1) facets that leads to the formation of ultrathin BiOCl nanosheets. Aside from these, the tailored facets growth of BiOCl nanosheets was also successfully achieved recently, by adjusting the pH of the hydrolytic solution with NaOH in hydrothermal route [24,25]. During the crystal growth process, the excess of OH^- may weaken the binding interaction of H^+ to terminal oxygen on the (0 0 1) surface of BiOCl, thus suppress the growth of (0 0 1) plane and promotes the appearance of {0 1 0} facets.

To tune the physicochemical properties and optimize the photoreactivity, there is still a rising demand for developing diverse growth techniques of shape-controlled BiOCl single crystals with specific facets exposed. Herein, we report the constrained growth of crystallographic {0 0 1} facets in single crystalline BiOCl nanodiscs with ultrasmall diameter (~65 nm) and extremely low percentage of {0 0 1} facets (~59%). The growth of BiOCl with adjustable percentage of exposed {0 0 1} facets at normal temperature and pressure (NTP) can be easily achieved under the assistance of hydroxylammonium chloride. Hydroxylammonium chloride solution here not only acts as a solvent, reductant and chloride donator, but also plays a core role on the constrained growth of {0 0 1} facets in BiOCl nanodiscs. To the best of our knowledge, such ultrasmall BiOCl nanodiscs with incredibly low percentage of {0 0 1} facets have never been reported. Additionally, the as-prepared BiOCl nanodiscs were found to exhibit enhanced sorption capacity and visible-light-induced photodegradation performance of Rhodamine B molecules.

2. Experimental

2.1. Materials

All chemicals used in the study were of reagent grade and applied without further purification. Sodium bismuthate hydrate ($NaBiO_3 \cdot 2H_2O$), hydroxylammonium chloride ($HONH_2 \cdot HCl$) and hydrochloric acid (HCl, 37 wt%) were used as reagents supplied by Sinopharm Chemical Reagent Co., Ltd. China. Rhodamine B chloride (RhB), rhodamine 110 chloride (Rh110) and rhodamine 19 perchlorate (Rh19) were purchased from Tianjin China Chemical Reagent Ltd., Exciton (USA) and Sigma–Aldrich (USA), respectively, and their structural formulas can be seen in Fig. S1. Deionized (DI) water was used in the whole experiment.

2.2. Preparation

BiOCl nanodiscs with minor percentage of {0 0 1} facets (denoted as BOC001-X, X = 59, 77 and 82) were synthesized through a facile oxidation-hydrolysis route, by using $NaBiO_3$ and $HONH_2 \cdot HCl$ as the starting materials. In a typical preparation, 1.2 g of $NaBiO_3$ was firstly suspended in 100 mL DI water under mag-

netic stirring. 30 mL freshly prepared $HONH_2 \cdot HCl$ solution with certain concentration was added dropwize to the suspension above. The yellow colored solid of $NaBiO_3$ was slowly converted to white precipitation within 24 h at room temperature. The solid sample was washed with DI water until the solution with neutral pH was obtained. The final product of BiOCl was dried at 60 °C in air for 24 h. BiOCl nanodiscs with 59%, 77% and 82% percentage of {0 0 1} facets can be prepared by using $0.58\,mol\,L^{-1}$, $2.88\,mol\,L^{-1}$ and $5.76\,mol\,L^{-1}$ hydroxylammonium chloride solution, respectively.

For comparison, micro-sized BiOCl nanosheets dominated with 95% {0 0 1} facets (denoted as BOC001-95) were also prepared via the oxidation-hydrolysis reaction between $NaBiO_3$ and hydrochloride solution (HCl, 37 wt%). Typically, 4 g $NaBiO_3$ was suspended into 50 mL DI water and then 20 mL HCl solution was added dropwise into the suspension until $NaBiO_3$ powder was dissolved completely. White precipitation of BOC001-95 was observed after adding 320 mL DI water into the solution. The sample was collected by centrifugation, washed thoroughly with water, and finally dried at 60 °C in air for 24 h.

2.3. Characterization and optical properties

The crystal structure of the samples was investigated using X-ray diffraction analysis (XRD, Rigaku X-ray diffractometer) with Cu Kα radiation. The morphologies and elemental compositions of as-prepared samples were examined by field-emission gun scanning electron microscope (FEG-SEM, FEI Inspect F50) equipped with an energy-dispersive X-ray spectroscope (EDS). Transmission electron microscopy (TEM) analysis was conducted on a FEI Tecnai F20 with a field emission gun and an accelerating voltage of 200 kV. XPS studies were carried out using a PHI 5000 VersaProbe spectrometer (UlVAC-PHI), employing Al Kα as the incident radiation source. The C_{1s} (E = 284.5 eV) level was served as the internal standard. The N_2 adsorption-desorption curves at liquid nitrogen temperatures (77.3 K) were measured on Micromeritics ASAP 2010 instrument. Fourier transform infrared spectra (FT-IR) were recorded at room temperature using a NEXUS 870 FTIR spectrometer (Nicolet). Raman measurement was carried out on a Horiba Jobin Yvon LabRAM HR 800 micro-Raman spectrometer with 514 nm excitation source at room temperature. The UV–vis absorption spectra of as-prepared solid samples were measured on Varian Cary 50 UV–Vis–NIR spectrophotometer via diffuse reflectance spectrum (DRS) mode, and pure $BaSO_4$ was employed as a reference.

2.4. Sorption performance

Batch sorption study was carried out to investigate the interfacial sorption kinetics and thermodynamics. 50 mg of BiOCl catalyst was mixed with 50 mL RhB aqueous solution with initial concentration of $9\,mg\,L^{-1}$, and the suspension was shaken in a shaking incubator at a constant speed (300 rpm) and temperature (286 K and 299 K). The suspensions were centrifuged at 3000 rpm after each batch adsorption experiment, and the concentration of RhB was calculated by measuring the absorbance at 554 nm using UV–vis spectrophotometer (Hitach U-3900). In all cases, the sorption process was carried out in dark, and the solution pH did not show apparent change before and after batch sorption.

2.5. Photoreactivity

In a typical photocatalytic experiment, appropriate dosage (D_{cat}) of as-prepared BiOCl sample was suspended in RhB solution with known initial concentration ($C_{0,RhB}$) and volume (V_{RhB}) in a glass reactor with a $33\,cm^2$ cross-section and 9 cm height. The reactor was then irradiated with visible light emitted from a Xenon lamp

(Beijing Trusttech Co., Ltd., CHF-XM) attached with a visible light filter that is able to filter out all other emission spectra except in the 400–800 nm region (the UV–vis transmittance spectrum of the light filter is depicted in Fig. S2). The concentration of RhB in centrifuged aqueous solution was monitored at 554 nm during the photodegradation process using a UV–vis spectrophotometer (Hitach U-3900). The *N*-deethylated intermediates were detected by an Alliance 2695HPLC (Waters) equipped with UV–vis diode array detector using a C18 inversed-phase column (Agilent Eclipse XDB-C18, 150 × 4.6 mm, 5 μm). Ammonium acetate and methanol were used as mobile phase, and a programmed gradient elution was conducted according to the method reported by Yu et al. [26]. The flow rate was 1.0 mL min^{-1}, and the injection volume was 50 μL.

2.6. Theoretical calculation [27,28]

The B3LYP and a $6 - 31 + G(d)$ basis set within the Gaussian 09 package was selected to optimize the Rhodamine B molecular
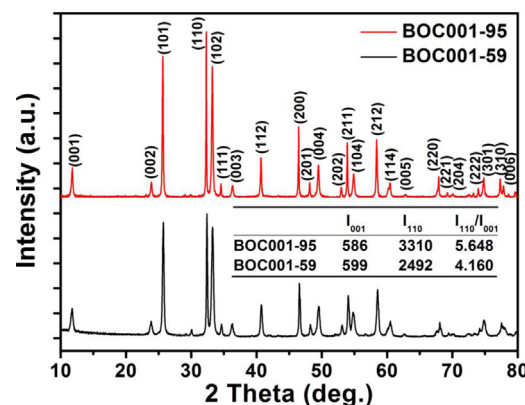

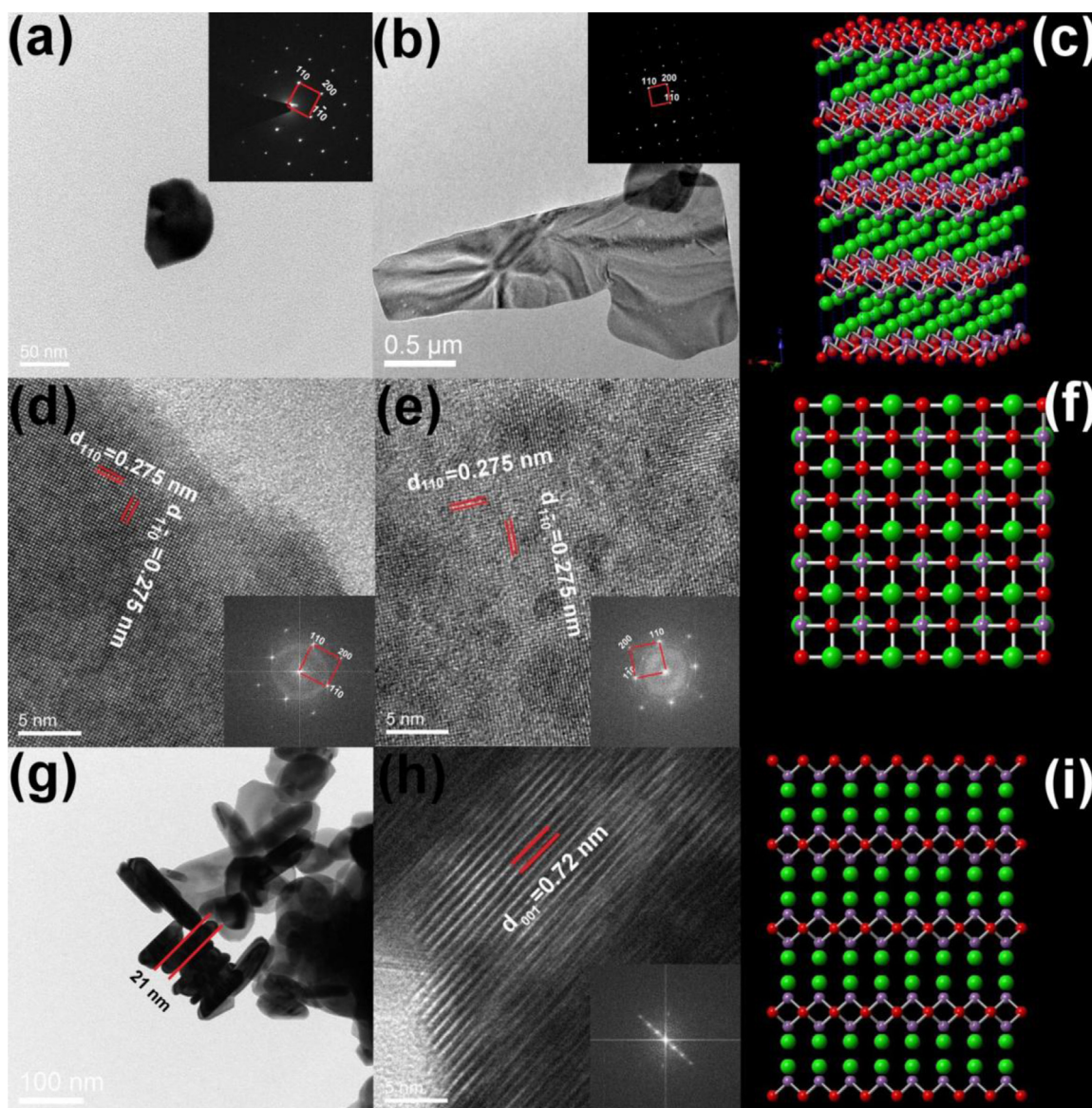**Fig. 1.** XRD patterns of as-prepared BOC001-59 and BOC001-95.

Fig. 2. Low mag TEM images and corresponding SAED patterns (inset) of a single BOC001-59 nanodisc (a) and BOC001-95 nanosheet (b); the 3D crystal structure (Bi, O and Cl atoms are purple, red and green balls, respectively) of BiOCl (c); HRTEM images and the corresponding Fourier transform (FT) spectra (inset) of the single BOC001-59 nanodisc (d) and BOC001-95 nanosheet (e) viewed along [0 0 1] zone axis; the crystal structure of BiOCl (0 0 1) orient (f); Low mag and HRTEM images and the corresponding FT spectra (inset) of BOC001-59 nanodisc viewed along the [1 1 0] BiOCl zone axis (g, h); the crystal structure of BiOCl (1 1 0) orient (i).

structure. The calculations for Bi^{3+} with hydroxylamine were performed by a density functional theory (DFT) method with B3LYP accompanied with mixed basis sets of a $6-31+G(d,p)$ set for H, O, N atoms and a lanl2dz set for Bi atom within the Gaussian 09 package. The $Bi^{3+} \longleftarrow ONH_3$ and $Bi^{3+} \longleftarrow NH_2OH$ system were optimized without any constraint in the beginning. The calculations on $Bi^{3+} \longleftarrow ONH_3$ and $Bi^{3+} \longleftarrow NH_2OH$ systems were considered in the ground state, where the total spin is zero. The calculations for the Bi^{3+} systems took two forms: (I) the hydroxylamine was coordinated to the metal via the nitrogen atom ($Bi^{3+} \longleftarrow NH_2OH$), and (II) coordination as the N-oxide via the oxygen atom $Bi^{3+} \longleftarrow ONH_3$). Both $Bi^{3+} \longleftarrow ONH^3$ and $Bi^{3+} \longleftarrow NH_20H$ systems were scanned on the basis of singled varied Bi—O bond length and Bi—N bond length separately, while the rest geometrical data were fixed without any change. The Bi—N bond and the Bi—O bond lengths varied from 1.5 to 2.9 Å by steps of 0.05 Å.

3. Results and discussion

3.1. Characterization

The XRD patterns of as-prepared BOC001-59 and BOC001-95 are depicted in Fig. 1. All of the diffraction peaks can be indexed to the tetragonal structure of BiOCl (space group:P4/nmm). The (0 0 1) peak at 11.75° is attributed to the periodic stacking structure among [Cl—Bi—O—Bi—O—Cl] layers along the *c*-axis, while the peak at 32.36° is assigned to the (110) plane, which is simultaneously perpendicular to (1 $\bar{1}$ 0) and (0 0 1) planes.

The average thickness (D_{001}, along [0 0 1] direction) of BOC001-95 and BOC001-59 was calculated using Debye–Scherrer formula, and the thicknesses were calculated at 26.8 nm and 21.2 nm, respectively. Interestingly, the BiOCl grew in hydroxylammonium chloride (BOC001-59) shows distinctive crystalline orientation with that grew in hydrogen chloride (BOC001-95). The diffraction intensity ratios of I_{110}/I_{001} were respectively estimated at 5.648 and 4.160 for BOC001-95 and BOC001-59, implying the constrained {0 0 1} facets and a relatively smaller size along the [1 1 0] crystallographic direction in BOC001-59 crystals. In other words, the crystal growth behavior along the *ab* plane is inhibited in the presence of hydroxylammonium chloride.

Low mag TEM images in Fig. 2 (a and b) show that the sizes of a typical BOC001-59 nanodisc and BOC001-95 nanosheet are approximately 65 nm and over 1 μm in width, respectively. The selected area electron diffraction (SAED) patterns show that both the nanodisc and nanosheet are single crystalline with tetragonal feature, which is consistent with the 3D crystal structure of BiOCl illustrated in Fig. 2c. HRTEM images of BOC001-59 and BOC001-95 as shown in Fig. 2(d and e), reveal that the interplanar spacing of 0.275 nm and the interfacial angle of 90° matched up with (1 1 0) and (1 $\bar{1}$ 0) types of lattice planes in tetragonal system of BiOCl (Fig. 2f). Fig. 2(g) illustrates an edge-on view of a piece of BOC001-59 nanodisc. The measured thickness of the BOC001-59 was ~21 nm, which is in agreement with the theoretical calculation via Debye–Scherrer formula (21.2 nm). The magnified view of the nanodisc edge in Fig. 2(h) shows that the interplanar d-spacing is 0.72 nm corresponding to the (0 0 1) lattice plane (Fig. 2i). Dark–field (DF) TEM images formed using diffraction spots from {1 1 0} and {2 0 0} planes show a strong bright contrast at the corner of the nanodisc (Fig. S3). Such non-uniform diffraction contrast in the DF-TEM image suggests the existence of strains or bending in BiOCl nanodiscs that drastically affects the diffraction behavior of electrons in the crystal. The produced strains or bending could be attributed to the deformation during the hydrolysis-based growth process in aqueous solution.

SEM characterization further confirmed the morphological features of as-prepared BiOCl samples. The depicted SEM image in
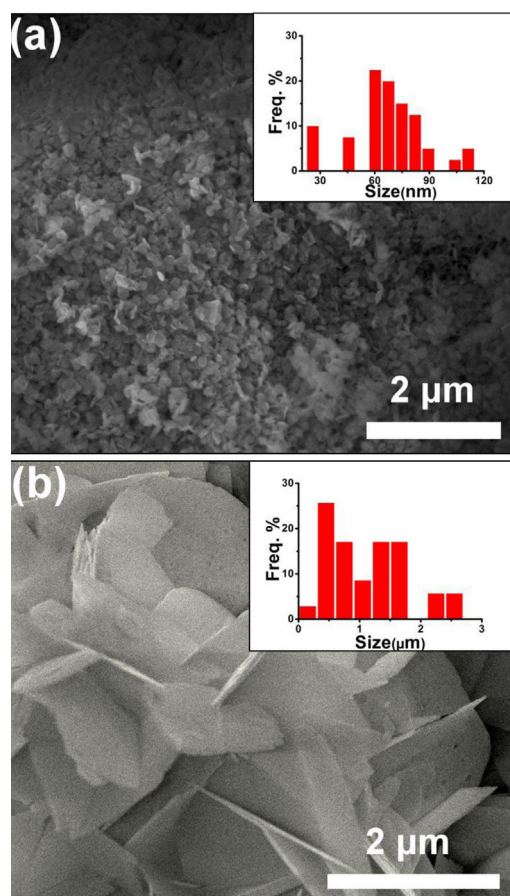

Fig. 3. Typical SEM images and the corresponding particle size distribution (inset, sample size = 50) of BOC001-59 (a) and BOC001-95 (b).

Fig. 3(a) clearly shows that the BOC001-59 was composed of a large amount of nanodiscs, which were centered at ~65 nm in width. The illustrated micrograph in Fig. 3(b) confirms the sheet-like large crystals (almost over 500 nm in width), and non-uniform size distribution in width for BOC001-95. On average, assuming 65 nm diameter and 21 nm thickness for each BOC001-59 nanodisc, while considering 1 μm diameter and 27 nm thickness for each BOC001-95 nanosheet, the statistically estimated percentage of the exposed {0 0 1} facets were found at 58.8% and 94.88%, respectively. The corresponding EDS results depicted in Fig. S4 suggest the stoichiometric molar ratio in both BiOCl samples.

The surface chemical states and composition of BOC001-59 were characterized by XPS analysis. From the XPS survey scan shown in Fig. 4(a), it can be found that bismuth, oxygen and chloride elements with molar ratio of 1:0.68:0.92 were semi-quantitatively identified, which are very close to the stoichiometric molar ratio in BiOCl. As shown in Fig. S5, no nitrogen containing species at BiOCl surface was detected by XPS, which indicates that the hydroxylammonium cations could not be firmly adsorbed on {0 0 1} and {1 1 0}/{1 $\bar{1}$ 0} facets preferentially. From high-resolution XPS spectra [16,29,30], as depicted in Fig. 4 (b–d), a typical $4f_{7/2}$ (158.8 eV) and $4f_{5/2}$ (164.2 eV) doublet in Bi_{4f} signal can be found apparently caused by the spin-orbit coupling effect, suggesting the tri-valence chemical state in BiOCl sample. The O_{1s} peak centered at 529.6 eV is attributed to the oxygen anions in Bi—O bond from the [—O—Bi—O—Bi—O—] slabs in BiOCl. In addition, typical characteristic doublet for chloride anions was observed at $2p_{3/2}$ (197.4 eV) and $2p_{1/2}$ (199.0 eV) in Cl_{2p} as well, which is referred to the typical characteristic of chloride anions.
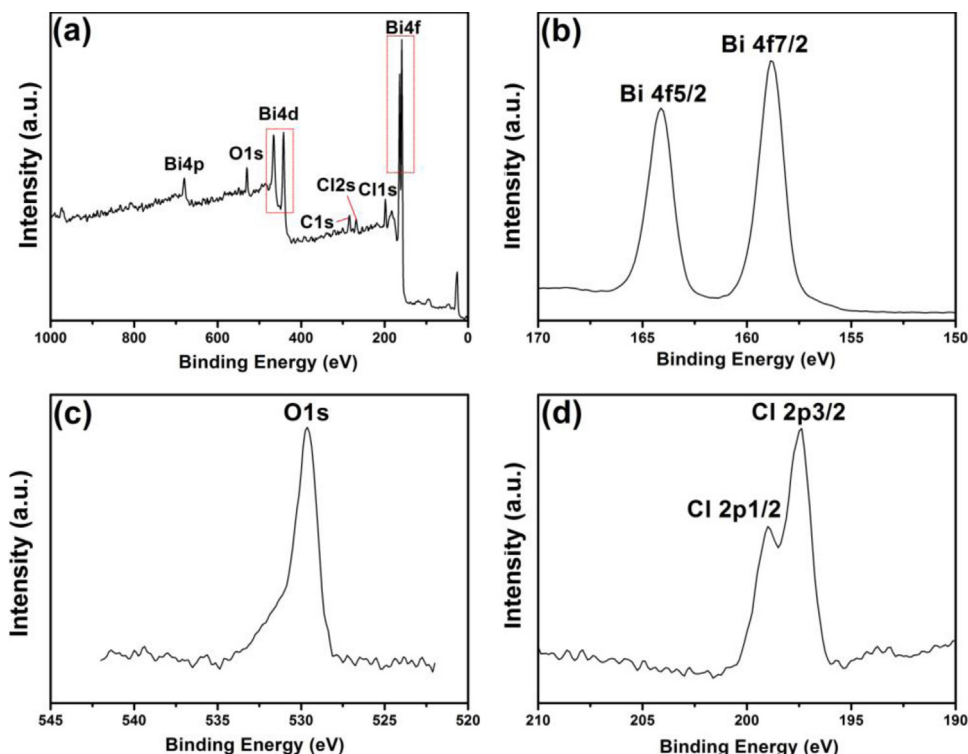
Fig. 4. XPS spectra of as-prepared BOC001-59: survey (a), Bi_{4f} (b), O_{1s} (c) and Cl_{2p} (d).

The specific surface area and porous structure of BOC001-59 and BOC001-95 were also compared and investigated. As depicted in Fig. 5(a), the adsorption "knee" at the early adsorption stage evidences the microporous structure inside BiOCl samples, which should be assigned to the stacking structure in BiOCl crystals. Owning to the much higher percentage of the {1 1 0} and $\{1\bar{1}0\}$ facets exposed in BOC001-59, the multi-layer adsorption

capacity on BOC001-59 which was fitted at $13.5\,m^2\,g^{-1}$ by means of BET model, exhibits almost three times as large as that of BOC001-95. The typical type-III curve with the capillary condensation at $P/P_0 = 0.96$ is observed for both BOC001-59 and BOC001-95, implying the possible existence of aggregated pores which correspond to the broad pore size distribution (as depicted in Fig. 5b). As shown in Fig. 5(c), the strongest IR absorption band at $520\,cm^{-1}$ is attributed
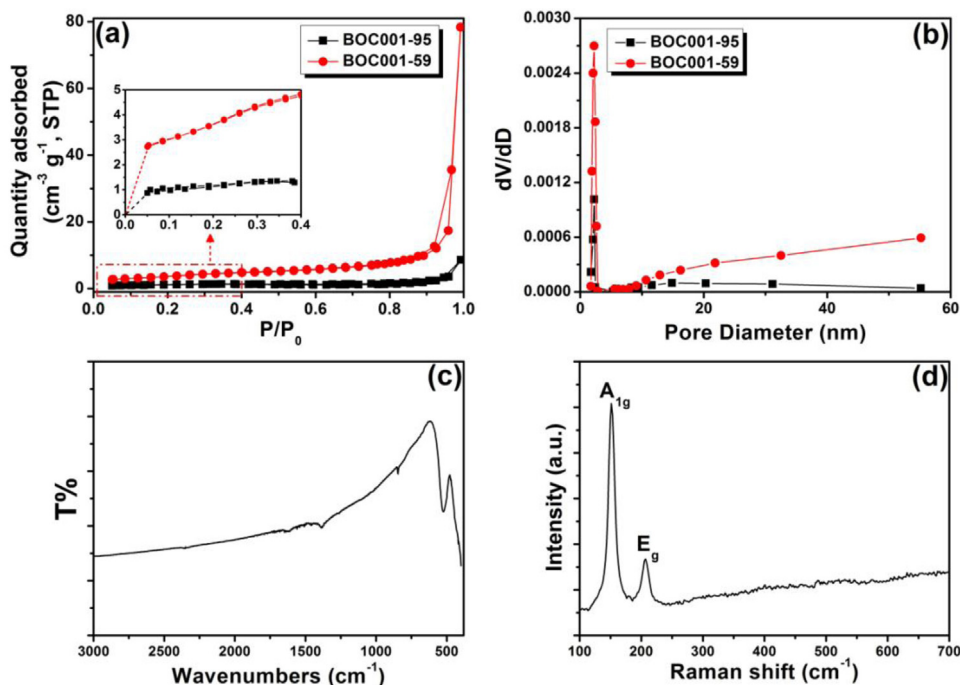

Fig. 5. N_2 adsorption-desorption isotherms (a) and the corresponding BJH pore size distribution curves calculated from absorption branch (b) of BOC001-59 and BOC001-95; FT-IR (c) and Raman spectra (d) of BOC001-59.

to the valent symmetrical A_{2u}-type vibrations of the Bi—O bond. While the absorption bands centered at $800\,cm^{-1}$, $1650\,cm^{-1}$ and $1400\,cm^{-1}$ can be assigned to the O—H bending vibrations [31]. The Raman bands shown in Fig. 5(d), at $144\,cm^{-1}$ and $201\,cm^{-1}$ can be attributed to the A_{1g} internal Bi—Cl stretching mode and E_g internal Bi—Cl stretching mode, respectively [32].

3.2. Crystal growth mechanism

Both the external conditions of crystallization and internal (structural) reasons may conclusively determine the external morphology of BiOCl nanocrystals. BiOCl crystallizes into a stacking structure characterized by $[Bi_2O_2]$ slabs interleaved with chloride atoms through van der Waals forces along the *c*-axis direction, however, stronger covalent interaction exist in the intralayer of $[Bi_2O_2]$. According to the periodic bond chain (PBC) theory, the crystal growth speed along one direction is strongly correlated with the bond intensity. Therefore BiOCl has a very high priority to crystallize in 2D structure. Of more interest to us is the possible formation mechanism of such growth constraint of $\{0\,0\,1\}$ facets in BiOCl nanodiscs. The dissociation equilibrium of hydroxylammonium chloride will occur in water as the strong acid with weak base reaction ($HONH_2 \cdot HCl \rightleftharpoons HONH_2 + HCl$). $NaBiO_3$ as a strong oxidizer was once applied in the fission of $\alpha\beta$-glycols to aldehydes or ketones in 1950 [33]. In the preparation process of BiOCl, bismuthate ion can be reduced to Bi^{3+} by both hydroxylamine and hydrogen chloride because of high oxidative ability of $NaBiO_3$ ($\phi^{\theta}(NaBiO_3/Bi^{3+}) = 1.8\,V$).

Hydroxylamine was once employed as a ligand to generate various complexes with metal cations [34,35], hence, it is reasonable to

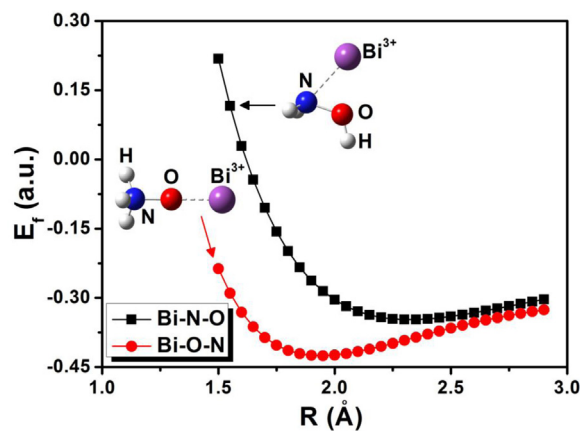**Fig. 6.** Formation energies (a.u.) for Bi^{3+} to hydroxylamine as functions of Bi—O distance (Å) in $[Bi–ONH_3]^{3+}$ and Bi-N distance (Å) in $[Bi-NH_2OH]^{3+}$.

speculate that the coordination between hydroxylamine and Bi^{3+} with $6s^2$ long pair might take place as well. The prediction has been verified theoretically by means of first principle calculations. It is well know that the formation energy can be defined as the difference between the sum of the energies for the isolated fragments and the total energies of the combined systems. Fig. 6 shows the formation energy as a function of Bi-X distance (X = N, O). The equilibrium distance between the Bi^{3+} and the N atom is about 2.3 Å while that between the Bi^{3+} and the oxygen is about 1.95 Å. It can be found that the formation energies of the Bi—O—N are much larger than those of Bi—N—O. The energy of Bi—O—N in each case has an energy lower
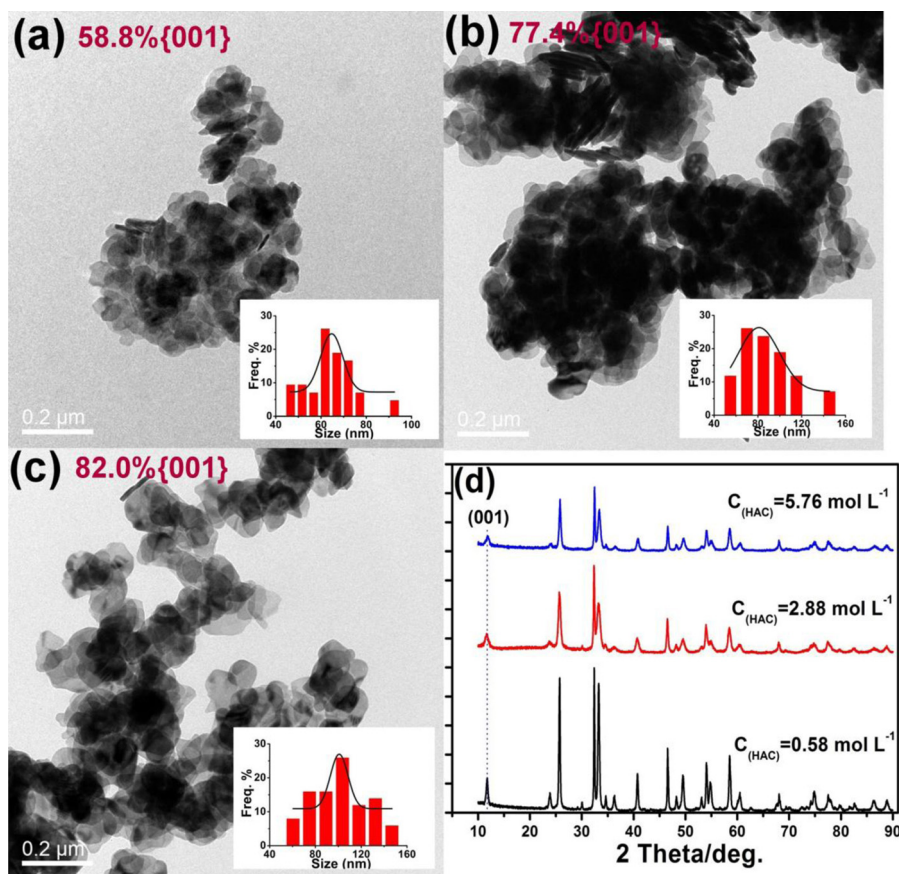

Fig. 7. TEM images (a–c) and the corresponding XRD patterns (d) of BOC001-59, BOC001-77 and BOC001-82 grew under different concentrations of hydroxylammonium chloride with $0.58\,mol\,L^{-1}$ (a, pH 3.13), $2.88\,mol\,L^{-1}$ (b, pH 2.56) and $5.76\,mol\,L^{-1}$ (c, pH 2.20). Insets of Fig. (a–c) depict the corresponding size distribution.

than those of Bi—N—O system, implying that the hydroxylamine is more inclined to coordinate to the oxygen atom that the nitrogen atom.

When the solute concentration went below the critical level, the nucleation of $[Bi–ONH_3]^{3+}$ complex would discontinue followed by the crystal growth in the presence of surrounding ions (Bi^{3+} cations, Cl^- anions and H_2O molecules). The Bi^{3+} dissociated from the coordinating complex, would participate in the hydrolysis process ($Bi^{3+} + H_2O + Cl^- = BiOCl + 2H^+$), and finally grew into the BiOCl nanodiscs at equilibrium concentration of the precipitation [36]. This is reason in our case that the whole hydrolysis process took almost 24 h to complete at room temperature (the XRD patterns of BiOCl prepared at different stages are depicted in Fig. S6). Consequently, the hydroxylammonium chloride solution selected can be referred to as a "four-in-one" reaction media. It not only acts as a kind of solvent, reductant and chloride donator, but also plays a crucial role on the constrained growth of {0 0 1} in BiOCl nanodiscs.

The efficient separation of nucleation and growth process (so called "two-stage growth") which involves an initially fast nucleation of amorphous particles and a subsequently slow aggregation and crystallization of particles [37,38], eventually results the formation of BiOCl nanodiscs with low percentage of exposed {0 0 1} facets. It is believable that the BiOCl nanodiscs with constrained {0 0 1} facets can be grown owning to both the coordination effect and the crystal growth thermodynamics features of BiOCl itself. On the other hand, the selective surface sorption of capping agents has been validated as an efficient way to grow faceted nanocrystals through adjusting surface energy in a crystal [38]. But it appears such mechanism may not be available in this case as proved by above-mentioned XPS analysis, possibly due to the mismatch of additive with facets in the solution environment.

3.3. Concentration effect of hydroxylammonium chloride

The concentration effect of hydroxylammonium chloride on the crystal growth behavior was also investigated. As depicted in Fig. 7, the increasing trend in particle size can be witnessed with the rise in concentration of hydroxylammonium chloride. When the concentration of hydroxylammonium chloride is 0.58 mol L^{-1}, BiOCl nanodiscs of 65 nm in diameter are resulted. However, ten-fold raise in the concentration of hydroxylammonium chloride expands the diameter to 101 nm of BiOCl nanodiscs. By means of Debye–Scherrer formula, the average thicknesses (D_{001}) of BOC001-77 and BOC001-82 were calculated at 11.8 nm and 11.1 nm, respectively. These results further suggest that the thickness slightly decreases with the rise of hydroxylammonium chloride concentration. The statistically estimated percentages of the exposed {0 0 1} facets were found at 77.4% and 82.0% for the BiOCl nanodiscs prepared in hydroxylammonium chloride with concentrations of 2.88 mol L^{-1} and 5.76 mol L^{-1}, respectively. HRTEM characterization confirms that the single crystalline BOC001-77 and BOC001-82 with bandgap of ∼3.3 eV expose the {0 0 1} facets only (as depicted in Fig. S7 and Fig. S8).
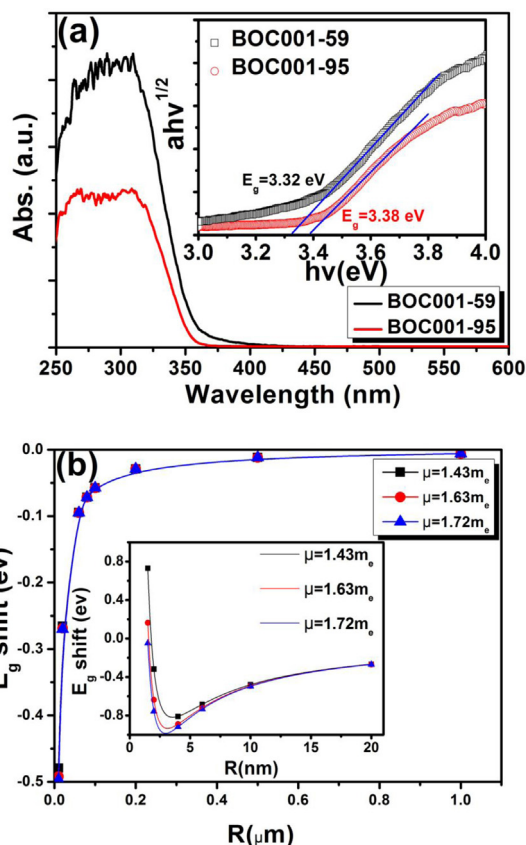

Fig. 8. UV–vis absorption spectra of BOC001-59 and BOC001-95 (a, inset shows the band gap determination) and changes of band gap shift as a function of width of BiOCl predicted by the Brus model at different reduced effective mass of exitions, $\mu = (1/m = 1/m_e + 1/m_h)$ and dielectric constant $\kappa = 6.74$ [39].

The large accumulation of H^+ inevitably suppresses the formation of $[Bi–ONH_3]^{3+}$ complex, which fasters the nucleation and growth process. On the other hand, the produced H^+ either from the hydrolysis of hydroxylammonium chloride or Bi^{3+} inclines to dangle at the oxygen terminated (0 0 1) surface, so that the oxygen can acquire enough electrons to fill their valence shells [24]. It is reasonable to believe that a growing number of H^+ cations will be anchored on the oxygen terminated (0 0 1) surface, with the rise in hydroxylammonium chloride concentration. Finally the crystal growth speed along the c-axis and ab plane is respectively inhibited and promoted, which explains the reason why the width and thickness of 2D structured BiOCl nanocrystals increases and declines with enlarging the concentration of hydroxylammonium chloride.

3.4. Optical properties

The band gap normally varies as the size changing of nanoscaled materials on the basis of Brus' EMM model [40]. Such effect

Table 1
Constants for the pseudo 1st -order and 2nd -order kinetics for RhB adsorption on BOC001-59 and BOC001-95 at 299 K and 286 K.

Catalyst	Temperature (K)	First-order kinetics			Second-order kinetics		
		k_1 (min^{-1})	q_{eq} (mg g^{-1})	r^2	k_2 (g mg^{-1} min^{-1})	v_0 (mg g^{-1} min^{-1})	r^2
BOC001-59	299	0.72	5.57	0.979	0.10	3.47	0.994
	286	0.62	6.96	0.973	0.06	3.38	0.994
BOC001-95	299	0.64	3.59	0.976	0.13	1.85	0.995
	286	0.43	5.45	0.985	0.05	1.75	0.997

Fig. 10. Changes of RhB concentration over BOC001-59 and BOC001-95 as a function of irradiation time (a, D_{cat} = 50 mg, $C_{0,RhB}$ = 9 mg L^{-1}, V_{RhB} = 200 mL) and the recycling runs for the photodegradation of RhB by BOC001-59 and BOC001-95 under visible light irradiation (b, D_{cat} = 50 mg, $C_{0,RhB}$ = 7.5 mg L^{-1}, V_{RhB} = 100 mL).
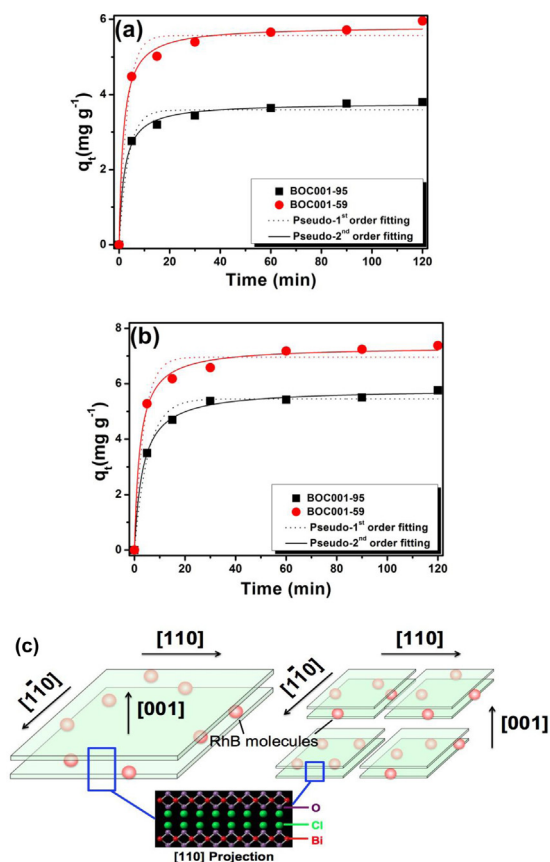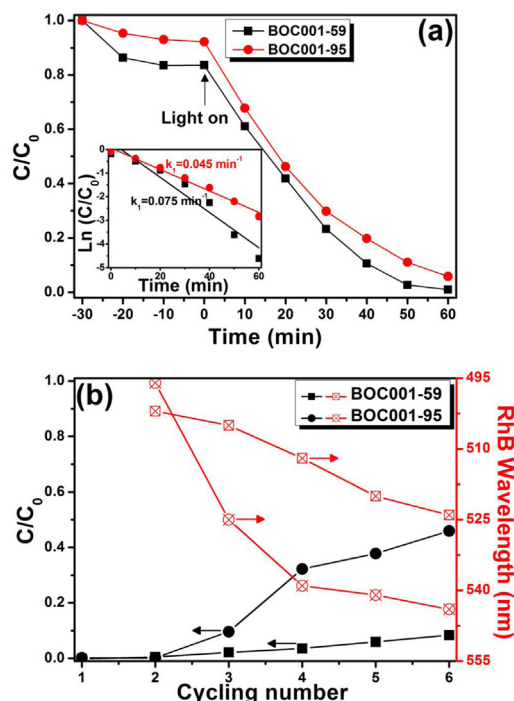
Fig. 9. Sorption kinetics of BOC001-59 and BOC001-95 for RhB (with initial pH 5) at 299 K (a) and 286 K (b); a schematic illustration of the enhanced sorption capacity onto BOC001-59 compared with BOC001-95 (c).

3.5. Sorption kinetics and thermodynamics

The sorption kinetics of BOC001-59 and BOC001-95 for RhB are depicted in Fig. 9a and b, respectively. The pseudo-second-order model can be used to fit all the sorption scatters well because of the relatively high correlation coefficients (r^2 = 0.99, Table 1). The sorption amounts at sorption equilibrium reach at 7.2 mg g^{-1} (286 K) and 5.7 mg g^{-1} (299 K) for BOC001-59, which exhibited significantly greater level of sorption capacity than BOC001-95: 5.7 mg g^{-1} (286 K) and 3.7 mg g^{-1} (299 K). That is, the sorption capacity of RhB on BOC001-59 is 1.26 and 1.54 times higher than that of BOC-95 at 286 K and 299 K, respectively. The cationic dye of RhB could be strongly adsorbed on the {0 0 1} facets with high oxygen density via the electrostatic interaction between positive charged ethylamine groups and oxygen anions [23]. BOC001-59 with a low percentage of exposed {0 0 1} facets may provide much more abundant sorption sites constructed by the interlayer spaces along the [0 0 1] direction. Assuming spherical shape, the cationic volume of an optimized RhB molecule (Fig. S9) was calculated at 1.219 nm^3 using the B3LYP/6 − 31 + G(d) method, hence the diameter of RhB molecule would be 1.326 nm. However, the interplanar spacing of d_{001} is only around 0.7 nm as confirmed by TEM and XRD analysis. Thus it is reasonable to believe that RhB molecules tend to aggregate at the mouth of the slots formed by the stacking of {0 0 1} facets, rather than intercalating inside the interplanar space (as depicted in Fig. 9c). That explains why the intraparti-

has been observed in 2D structured BiOCl system as well. In a typical study carried out by Song et al. [21], the bandgap of as-prepared ultrathin BiOCl nanosheets was measured at 3.54 eV, which is wider than that of bulk BiOCl (3.4 eV). However, Xiong et al. [4] reported a contrary tendency, i.e., the bandgap of as-prepared square-like BiOCl, having 100–200 nm width and 20–30 nm thickness, was slightly smaller than that of microsized commercial BiOCl samples, which might be possibly owning to the phonon confinement effect. In our study, DRS was employed to investigate the optical absorption of as-prepared BiOCl samples (as depicted in Fig. 8a). By using a classical Tauc's approach, the optical band gaps of BOC001-59 and BOC001-95 were measured at 3.32 eV and 3.38 eV, respectively. Fig. 8(b) depicts the changes of band gap shift as a function of diameter of 2D structured BiOCl, which was plotted via Brus'EMM model. It can be found that the band gap decreases marginally (ΔE equals to −0.094 eV and −0.006 eV at 60 nm and 1 μm in diameter, respectively) as the decline of diameter of 2D structured BiOCl from 1 μm to 4 nm. Whereas further decreasing the diameter from such critical size may lead to the rising of band gap energy. Thus the determined band gap values agree well with the predicted results by Brus'EMM model.

Table 2
Thermodynamic parameters for the adsorption of RhB on BOC001-59 and BOC001-95 at 299 K and 286 K.

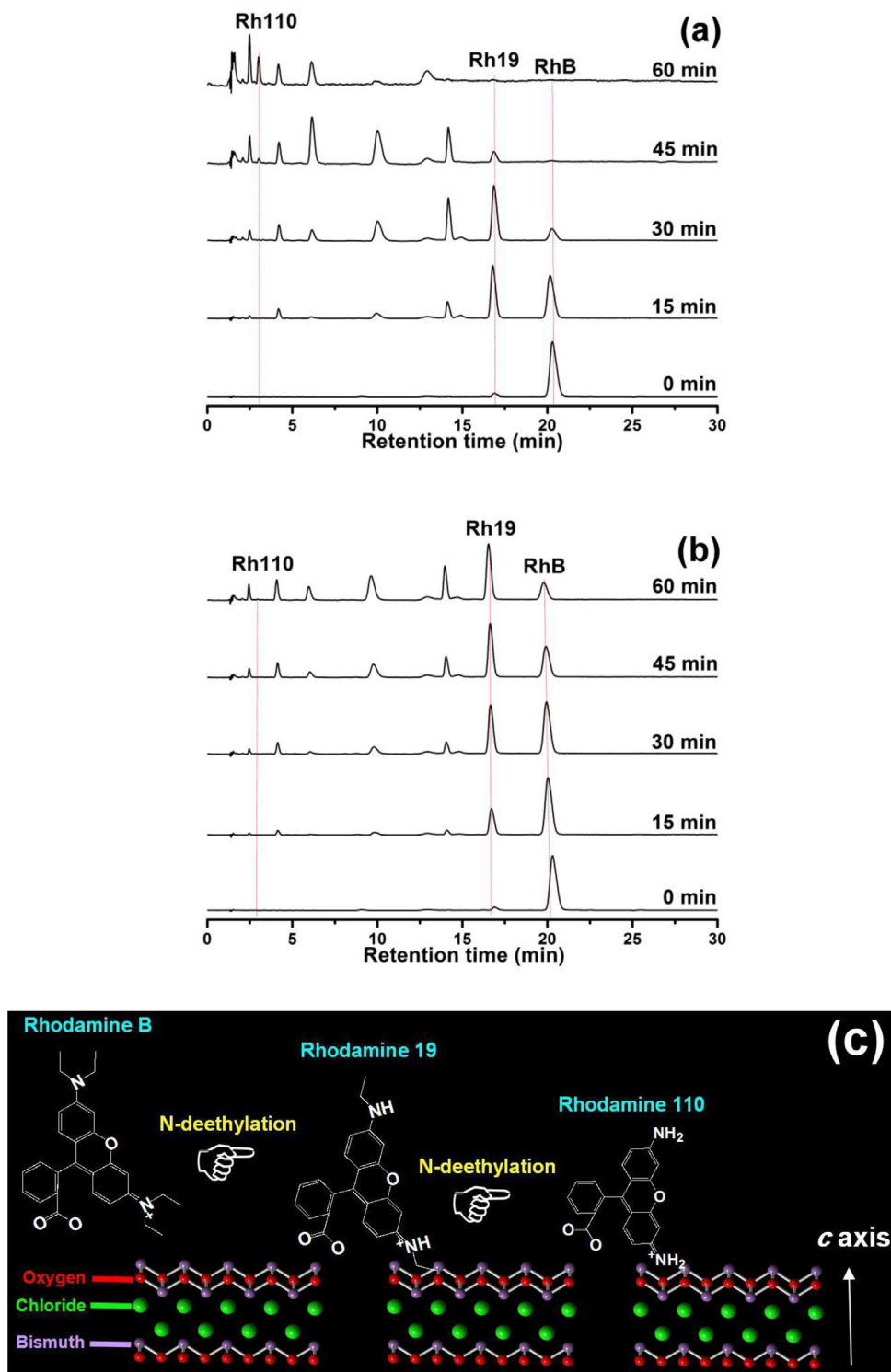| Catalyst	Temperature (K)	K	ΔG° (kJ mol^{-1})	ΔH° (kJ mol^{-1})	ΔS° (J mol^{-1} K^{-1})
BOC001-59	299	0.1836	4.22	−16.11	−67.93
	286	0.2464	3.33		
BOC001-95	299	0.1098	5.49	−26.44	−106.76
	286	0.178	4.11		

Fig. 11. HPLC graphs of RhB aqueous solution undergoing photodegradation on BOC001-59 (a) and BOC001-95 (b) at various reaction time (D_{cat} = 50 mg, $C_{0,RhB}$ = 9 mg L^{-1}, V_{RhB} = 200 mL), and the proposed *N*-deethylated pathway of RhB over BiOCl with low percentage of exposed {0 0 1} facets under visible light irradiation (c). (For interpretation of the references to color in this figure legend, the reader is referred to the web version of this article.)

cle diffusion is not the rate-controlling step in terms of the fitting results by intraparticle diffusion model (as depicted in Fig. S10). In addition, the sorption thermodynamic parameters of free energy changes (ΔG°), enthalpy changes (ΔH°) and entropy changes (ΔS°), were calculated based on the sorption kinetics results obtained at different temperatures (Table 2). A dramatic decline in saturated sorption capacity from kinetics data, was observed by increasing the temperature from 286 K to 299 K on both BOC001-59 and

BOC001-95, indicating the exothermic nature in the sorption process. The negative ΔH° value also confirmed exothermic nature, and the positive ΔG° value indicated the non-spontaneity of the sorption process. In a typical sorption process, the RhB molecules repeatedly undergo external and intraparticle diffusion until they finally adsorbed at the active sites on BiOCl [41]. The degree of RhB molecular movement decreases from three-dimension (in bulk solution) to two-dimension (on BiOCl surface), or even to one-

dimension (inside {0 0 1} interplanar spaces) during the sorption process, resulting the negative ΔS° value calculated.

3.6. Photoreactivity driven by visible light

The visible-light-induced photodegradation of RhB dye over wide-band gap semiconductor of BiOCl has been extensively confirmed in terms of photosensitization mechanism [23,42]. Fig. 10(a) depicts the variation of RhB concentration in the presence of BOC001-59 and BOC001-95 under visible light exposure. BiOCl cannot be excited directly under visible light due to its wide energy gap. However, it can be used as a semiconducting media (electron acceptor and donator) in photosensitized degradation of some special dyes under visible light irradiation. After an hour exposure, it can be found that 100% and 94% degradation of model contaminant can be observed with BOC001-59 and BOC001-95, respectively. In addition, the as-prepared BOC001-59 exhibited superior reaction kinetic constant 1.7 times greater than that conventional BOC001-95 dominated with {0 0 1} facets. Controlled experiments suggest that no decomposition of RhB was resulted in the absence BiOCl sample under visible light irradiation. Around 16% and 8% of RhB molecules could be absorbed by BOC001-59 and BOC001-95 in dark under identical operation conditions, respectively. The corresponding time-dependent UV–vis spectra depicted in Fig. S11 suggest that absorbance of the absorption peak at 554 nm decreases intensely as the photodegradation reaction proceeded. Meanwhile, it is noteworthy that the wavelength of the characteristic absorption peak of RhB centered at 554 nm finally shifts to shorter wavelength of 500 nm and 523 nm in the presence of BOC001-59 and BOC001-95, respectively, revealing that a higher efficiency for the N-deethylation process might occur on BOC001-59 [43–45].

Moreover, as depicted in Fig. 10(b), the as-prepared BOC001-59 was found to be considerably photoreactive even after the sixth cycling run, where 92% degradation was observed. The absorption band of RhB at visible region shifts to 524 nm ultimately. However, the photodegradation performance greatly decays on BOC001-95 dominated with {0 0 1} facets since the third run. Only around 54% of photodegradation was achieved, and the absorption band of RhB finally shifted to 543 nm after the sixth run (Fig. S12). XRD results further prove the well-maintained crystallographic structure of as-prepared BiOCl samples after the sixth run (Fig. S13). The above-mentioned results unambiguously show that the BiOCl nanodiscs with low percentage {0 0 1} exposed are beneficial for the photoactivity improvement. It is well known that the efficient uptake between the dye molecules and photocatalyst is crucial for the transfer of photogenerated electrons to the conduction band of photocatalyst [24]. Thus the improved photosensitization activity over BiOCl nanodiscs with low percentage {0 0 1} exposed, can be accounted for the substantially enhanced sorption capacity through providing much richer sorption active sites along the [001] direction. On the other hand, a recent study carried out by Ding et al. also suggested that the density of exposed oxygen on {0 0 1} facets which may lead to the higher oxygen vacancy concentration, could also promote the photosensitization performances via a possible second transfer of electrons [46]. In our study, however, the BiOCl001-59 with much lower percentage of exposed {0 0 1} still exhibited superior activity to BiOCl001-95, indicating that the direct interfacial contact between dye molecules and semiconductor may matter more than exposed oxygen vacancy concentration.

HPLC analysis was employed to further investigate the possible degradation pathways. As presented in Fig. 11, it can be found that the chromatographic peak intensity of RhB molecules (at retention time of 20.4 min, Fig. S14) is weakened dramatically after photodegradation over BOC001-59 with low percentage of exposed {0 0 1} facets, and new chromatographic peaks with differ-ent retention times appear at the mean time, implying that the RhB molecules were efficiently decomposed and new molecules were formed in the photosensitization process. As depicted in Fig. 11(a), Rh19 molecules identified at retention time of 17.7 min are firstly detected within 15 min, followed by the complete decomposion after 60 min. Meanwhile, Rh110 molecules at retention time of 3.0 min are also detected ever since the degradation of Rh19. Therefore, the degradation of RhB onto BOC001-59 underwent a stepwise N-deethylation process until the formation of Rh110. However, conventional BOC110-95 dominated with {0 0 1} facets suggests inferior photoreactivity. As shown in Fig. 11 (b), Rh110 can not be detected in the photodegradation over BOC110-95, and Rh19 molecules are also enriched as the reaction proceeds. A tentative N-deethylated pathway of RhB is proposed in Fig. 11(c), based on the above-mentioned experimental results and the previous lieteratures. First, due to the high oxygen atom density on the {0 0 1} facets, RhB molecules would be preferentially anchored on the {0 0 1} facets via the electrostatic interaction between ethylamine groups and oxygen anions [23]; Second, under visible-light-induced photosensitization process [47–49], as an ethyl group eliminated from RhB molecules, a positive center would form at the single ethyl side because of the transfer of electron atmosphere [26]. Thereby, the single ethyl side is much more preferentially to be up took by BiOCl; Third, four ethyl groups would be eliminated successively until the formation of fully N-deethylated RhB (Rh110). Eventually, the cleavage of the whole conjugated chromophore structure in RhB might dominate the photodegradation process since the N-deethylation process [26].

4. Conclusions

To sum up, ultrasmall BiOCl nanodiscs with 59% of exposed {0 0 1} facets have been successfully synthesized. As the plentiful sorption sites afforded by the interlayer spaces along the [0 0 1] direction, the as-prepared BiOCl nanodiscs exhibit much higher sorption capacity and photosensitization degradation activity than conventional BiOCl nanosheets dominated with {0 0 1} facets. These contributions not only developed a facile synthetic route of BiOCl with superior performance, but also shed light on the better understanding of tailored synthesis of BiOCl as well as other 2D structured catalysts with defined surface properties.

Appendix A. Supplementary data

Supplementary data associated with this article can be found, in the online version, at http://dx.doi.org/10.1016/j.apcatb.2015.03.047.

References

[1] M.R. Hoffmann, S.T. Martin, W.Y. Choi, D.W. Bahnemannt, Chem. Rev. 95 (1995) 69–96.
[2] T. Schneider, M. Matsuoka, M. Takeuchi, J.L. Zhang, Y. Horiuchi, M. Anpo, D.W. Bahnemann, Chem. Rev. 114 (2014) 9919–9986.
[3] J.C. Colmenares, R. Luque, Chem. Soc. Rev. 43 (2014) 765–778.
[4] J.Y. Xiong, G. Cheng, G.F. Li, F. Qin, R. Chen, RSC Adv. 1 (2011) 1542–1553.
[5] J. Li, Y. Yu, L.Z. Zhang, Nanoscale 6 (2014) 8473–8488.

[6] F. Chen, H.Q. Liu, S. Bagwasi, X.X. Shen, J.L. Zhang, J. Photochem. Photobiol. A: Chem. 215 (2010) 76–80.
[7] A. Luz, J. Conradt, M. Wolff, H. Kalt, C. Feldman, Solid State Sci. 19 (2013) 172–177.
[8] K. Li, Y.L. Xu, Y. He, C. Yang, Y.L. Wang, J.P. Jia, Environ. Sci. Technol. 47 (2013) 3490–3497.
[9] J.L. Yuan, J. Wang, Y.Y. She, J. Hu, P.P. Tao, F.C. Lv, Z.G. Lu, Y.Y. Gu, J. Power Sources 263 (2014) 37–45.
[10] X.Y. Zhao, Z.X. Zhao-Karger, D. Wang, M. Fichtner, Angew. Chem. Int. Ed. 52 (2013) 13621–13624.
[11] K.L. Zhang, C.M. Liu, F.Q. Huang, C. Zheng, W.D. Wang, Appl. Catal. B: Environ. 68 (2006) 125–129.
[12] H.Z. An, Y. Du, T.M. Wang, C. Wang, W.C. Hao, J.Y. Zhang, Rare Met. 27 (2008) 243–250.
[13] Z.T. Deng, D. Chen, B. Peng, F.Q. Tang, Cryst. Growth Des. 8 (2008) 2995–3003.
[14] L.Y. Zhu, Y. Xie, X.W. Zheng, X. Yin, X.B. Tian, Inorg. Chem. 41 (2002) 4560–4566.
[15] X. Zhang, Z.H. Ai, F.L. Jia, L.Z. Zhang, J. Phys. Chem. C 112 (2008) 747–753.
[16] L.P. Zhu, G.H. Liao, N.C. Bing, L.L. Wang, Y. Yang, H.Y. Xie, CrystEngComm 12 (2010) 3791–3796.
[17] X.C. Zhang, X.X. Liu, C.M. Fan, Y.W. Wang, Y.F. Wang, Z.H. Liang, Appl. Catal. B: Environ. 132–133 (2013) 332–341.
[18] X. Zhang, X.B. Wang, L.W. Wang, W.K. Wang, L.L. Long, W.W. Li, H.Q. Yu, ACS Appl. Mater. Interfaces 6 (2014) 7766–7772.
[19] A. Biswas, R. Das, C. Dey, R. Banerjee, P. Poddar, Cryst. Growth Des. 14 (2014) 236–239.
[20] J. Di, J.X. Xia, S. Yin, H. Xu, L. Xu, Y.G. Xu, M.Q. He, H.M. Li, RSC Adv. 4 (2014) 14281–14290.
[21] J.M. Song, C.J. Mao, H.L. Niu, Y.H. Shen, S.Y. Zhang, CrystEngComm 12 (2010) 3875–3881.
[22] J.M. Ma, X.D. Liu, J.B. Lian, X.C. Duan, W.J. Zheng, Cryst. Growth Des. 10 (2010) 2522–2527.
[23] D.H. Wang, G.Q. Gao, Y.W. Zhang, L.S. Zhou, A.W. Xu, W. Chen, Nanoscale 4 (2012) 7780–7785.
[24] J. Jiang, K. Zhao, X.Y. Xiao, L.Z. Zhang, J. Am. Chem. Soc. 134 (2012) 4473–4476.
[25] S.X. Weng, J. Hu, M.L. Lu, X.X. Ye, Z.X. Pei, M.L. Huang, L.Y. Xie, S. Lin, P. Liu, Appl. Catal. B: Environ. 163 (2015) 205–213.
[26] K. Yu, S.G. Yang, H. He, C. Sun, C.G. Gu, Y.M. Ju, J. Phys. Chem. A 113 (2009) 10024–10032.
[27] A.D. Becke, J. Chem. Phys. 98 (1993) 5648–5652.
[28] B. Miehlich, A. Savin, H. Stoll, H. Preuss, Chem. Phys. Lett. 157 (1989) 200–206.
[29] L. Armelao, G. Bottaro, C. Maccato, E. Tondello, Dalton Trans. 41 (2012) 5480–5485.
[30] G. Cheng, J.Y. Xiong, F.J. Stadler, New J. Chem. 37 (2013) 3207–3213.
[31] Z.T. Deng, F.Q. Tang, A.J. Muscat, Nanotechnology 19 (2008) 295705.
[32] S.H. Cao, C.F. Guo, Y. Lv, Y.J. Guo, Q. Liu, Nanotechnology 20 (2009) 275702.
[33] W. Rigby, J. Chem. Soc. 1950 (1950) 1907–1913.
[34] M.N. Hughes, Inorg. Chim. Acta 18 (1976) 69–76.
[35] K. Wieghardt, K. Quilitzsch, J. Weiss, Inorg. Chim. Acta 89 (1984) 43–45.
[36] C. Burda, X.B. Chen, R. Narayanan, M.A. El-Sayed, Chem. Rev. 105 (2005) 1025–1102.
[37] L.S. Zhong, J.S. Hu, H.P. Liang, A.M. Cao, W.G. Song, L.J. Wan, Adv. Mater. 18 (2006) 2426–2431.
[38] G. Liu, J.C. Yu, G.Q. Lu, H.M. Cheng, Chem. Commun. 47 (2011) 6763–6783.
[39] L.J. Zhao, X.C. Zhang, C.M. Fan, Z.H. Liang, P.D. Han, Physica B 407 (2012) 3364–3370.
[40] H. Lin, C.P. Huang, W. Li, C. Ni, S.I. Shah, Y.H. Tseng, Appl. Catal. B: Environ. 68 (2006) 1–11.
[41] Q. Yu, R.Q. Zhang, S.B. Deng, J. Huang, G. Yu, Water Res. 43 (2009) 1150–1158.
[42] J.L. Hu, W.J. Fan, W.Q. Ye, C.J. Huang, X.Q. Qiu, Appl. Catal. B: Environ. 158–159 (2014) 182–189.
[43] G. Liu, X. Li, J. Zhao, H. Hidaka, N. Serpone, Environ. Sci. Technol. 34 (2000) 3982–3990.
[44] F. Chen, J.C. Zhao, H. Hidaka, Int. J. Photoenergy 5 (2003) 209–217.
[45] Q. Wang, C.C. Chen, D. Zhao, W. Ma, J.C. Zhao, Langmuir 24 (2008) 7338–7345.
[46] L.Y. Ding, R.J. Wei, H. Chen, J.C. Hu, J.L. Li, Appl. Catal. B: Environ. 172–173 (2015) 91–99.
[47] X.M. Mao, C.M. Fan, Y.W. Wang, Y.F. Wang, X.C. Zhang, Appl. Surf. Sci. 317 (2014) 517–525.
[48] H.Y. Hao, Y.Y. Xu, P. Liu, G.Y. Zhang, Chin. Chem. Lett. 26 (2015) 133–136.
[49] J.S. Cheng, C. Wang, Y.F. Cui, Y. Sun, Y. Zuo, J. Mater. Sci. Technol. 30 (2014) 1130–1133.